

Visualization of electrolyte flow in vanadium redox flow batteries using synchrotron X-ray radiography and tomography – Impact of electrolyte species and electrode compression

Nico Bevilacqua ^a, László Eifert ^a, Rupak Banerjee ^a, Kerstin Köble ^a, Tomáš Faragó ², Marcus Zuber ², Aimy Bazylak ³, Roswitha Zeis ^{a,d,*}

^a Karlsruhe Institute of Technology (KIT), Helmholtz Institute Ulm (HIU), Helmholtzstraße 11, 89081, Ulm, Germany

² Karlsruhe Institute of Technology (KIT), Institute for Photon Science and Synchrotron Radiation (IPS), Hermann-von-Helmholtz-Platz 1, 76344, Eggenstein-Leopoldshafen, Germany

³ Thermofluids for Energy and Advanced Materials (TEAM) Laboratory, Department of Mechanical & Industrial Engineering, University of Toronto, Institute for Sustainable Energy, Faculty of Applied Science & Engineering, University of Toronto, 5 King's College Road, Toronto, Ontario, M5S 3G8, Canada

^d Karlsruhe Institute of Technology (KIT), Institute for Physical Chemistry, Fritz-Haber-Weg 2, 76131, Karlsruhe, Germany



HIGHLIGHTS

- Liquid electrolyte progression front through porous electrode.
- X-ray tomography shows the occurrence and displacement of air bubbles.
- Wettability of carbon felt electrode plays a major role in saturation.
- V(III) exhibits the highest saturation.
- Quantitative study shows compression dominates pressure drop vs. vanadium species.

ARTICLE INFO

Keywords:

Synchrotron
X-ray radiation
Porous electrode
Electrolyte distribution
Vanadium redox flow battery
Wetting behavior

ABSTRACT

The electrolyte distribution inside the porous electrodes of vanadium redox flow batteries is critical to the performance, as it determines the electrochemically active surface area. Herein, the influence of thermal activation, compression, and the injected electrolyte species on the pressure drop and the wetting is investigated by means of synchrotron X-ray radiation. The saturation versus the through-plane position is quantitatively displayed as a function of time to resolve the wetting process. The initial state after the imbibition is then quantitatively compared to the saturation after flow-through conditions. It was concluded that thermal activation plays a major role in the wetting, resulting in an up to six times higher saturation. Only a minor increase in saturation between the initial wetting state and after flow-through was observed. Additionally, there are only minor differences in the wetting behavior between the vanadium species in the electrolyte, the V(III) electrolyte shows the highest saturation. Increasing compression leads to a higher pressure drop and the saturation decreases only at compression ratios higher than 50%. Air pocket formation inside the liquid column was observed and the displacement and re-emergence of air pockets after flow-through is displayed.

1. Introduction

Over the past decades, Vanadium Redox Flow Batteries (VRFBs) have gained considerable attention as the implementation of renewable energies into the grid demands the availability of peak-shaving technologies, such as large-scale batteries to ensure the stability of the grid [1].

One particular advantage of an RFB is the decoupling of energy capacity and power density. The amount of stored energy is based on the size of the tanks, whereas the power density depends on the active area of the battery stack [2,3].

The redox reactions, which convert energy inside the VRFB, take place on the surface of a porous carbon electrode, through which the

* Corresponding author. Karlsruhe Institute of Technology (KIT), Helmholtz Institute Ulm (HIU), Helmholtzstr. 11, 89081 Ulm, Germany.

E-mail address: roswitha.zeis@kit.edu (R. Zeis).

<https://doi.org/10.1016/j.jpowsour.2019.227071>

Received 16 May 2019; Received in revised form 22 August 2019; Accepted 25 August 2019

Available online 5 September 2019

0378-7753/© 2019 The Authors. Published by Elsevier B.V. This is an open access article under the CC BY-NC-ND license

(<http://creativecommons.org/licenses/by-nc-nd/4.0/>).

electrolyte is pumped or transported by diffusion, depending on the flow field design [4]. Flow-through operation means that the electrolyte is forced through the porous electrode by disconnected or absent flow channels, whereas flow-by operation implies connected flow channels. In flow-by mode, the electrolyte transport into the electrode happens mostly due to diffusion. Thus, the wettability of the carbon electrode is critical to the performance of the battery, as it determines the electrochemically active surface area (ECSA) [5,6]. Visualizing the flow behavior inside the porous electrodes is vital to understand the loss mechanisms and to optimize the performance [7]. While a larger ECSA allows a higher reaction rate, optimizing the mass transport ensures that the reactants are transported to the reaction sites quickly. This simultaneously decreases the pumping losses of the battery, increasing the overall efficiency of the system [8–11].

Optically transparent cells can be employed to visualize the flow on the surface of the porous electrode and track the reaction by redox-active fluorescence of trace molecules via Ultraviolet–Visible light (UV–Vis) spectroscopy in a two dimensional way [12]. A three-dimensional approach using photons which cannot penetrate the electrode requires a complicated cell design, favoring methods with photons able to pass through an enclosed cell. X-rays and neutron beams are able to visualize an enclosed cell, resolve the structure of the porous electrodes, and trace the flow inside the pore space using neutron or X-ray radiography and tomography. However, tracking the reaction locally is difficult with these methods, as they are unable to locally distinguish between reaction educts and products. Three-dimensional techniques enable an insight into the fluid dynamics and the mass transport of the reactants inside the opaque electrodes from the supply channels to the electrochemically active sites and can resolve restrictions in liquid movement inside the porous carbon felts. The flow behavior of the electrolyte inside the porous electrode is closely related to the liquid water transport in a polymer electrolyte membrane fuel cell (PEMFC), thus parallels can be drawn between the experimental approach in this field and in the field of VRFBs. Flow behavior of PEMFCs has already been studied by various groups using neutron [13, 14] and X-ray based [15–22] techniques and to complement the visualization of the flow behavior, multiple modeling approaches have been performed in recent years [23–25]. They offer a well-suited approach to the study of redox flow batteries, especially regarding the validity of these methods [26,27].

Trogadas et al. recently highlighted the importance of X-ray tomography, especially in combination with X-ray photoelectron spectroscopy (XPS), when examining the degradation processes in the VRFB electrode [28]. They revealed fiber agglomeration and carbon oxidation using reconstructed 3D X-ray micro tomography images and XPS. Jervis et al. applied X-ray computed tomography to investigate the influence of compression on the structure of commercially available carbon felt electrodes with respect to fiber-fiber contact, porosity changes throughout the electrode, and the tortuosity of the carbon felt. They report a non-uniform porosity profile under compression with a lower porosity at the compressing sides [21]. Greco et al. investigated porous carbon electrodes, which were pretreated at different temperatures and applied X-ray tomography to investigate the influence of the activation temperature on the structure and changes in wettability of the electrode [5]. They found opposing trends, as the ECSA decreases with increasing thermal activation temperature, which has a negative effect on the performance of the cell. However, the higher surface oxygen content is beneficial to the wetting properties of the electrodes. They conclude an optimum activation temperature at 475 °C. Eifert et al. present a detailed XPS study of the surface structure of a carbon felt electrode and conclude that the surface oxygen content decreases from 24% to 19% and that the nature of the carbon-oxygen bond shifts toward single bond during thermal pre-treatment [29]. Tariq et al. applied X-ray tomography to discern the wetting behavior of electrolyte inside a previously dry carbon paper and found that a strong anisotropy of fibers leads to an uneven progression front in the form of preferred liquid pathways along

the electrode fibers, leaving large pore spaces dry even under pressurized flow, which might accelerate the local degradation [22]. Further, neutron-based radiography has been performed on VRFBs by J. T. Clement, who applied this technique to locally investigate the performance and the mass transport limitation of various electrode materials and to visualize gas evolution [30].

Additionally, the pressure drop in a redox flow battery is a useful parameter to determine the overall efficiency of a system, as it is a direct measure of one part of the parasitic pumping losses. A lower pressure drop leads to lower pumping losses, which decreases the ancillary losses of the stack [31,32]. The influence of several parameters on the pressure drop was studied by various groups [10,33–37]. Xu et al. compared redox flow batteries with and without a flow field and showed that the pressure drop at lower flow rates is lower in the presence of an engineered flow field [10]. They further presented a detailed modeling study about the State of Charge (SoC) dependent dynamic viscosity change of the electrolytes in both half-cells and modeled a decreasing pressure drop for an increasing SoC [37]. Latha et al. present data on the temperature dependence of the pressure drop and show that the pressure drop decreases at higher temperatures due to a lower electrolyte viscosity [38] and together with Reed et al., they conclude that the interdigitated flow field design is beneficial for a flow-through system [34]. Houser et al. presented an extensive evaluation of the influence of the flow field architecture on the performance, the pumping loss, and the overall efficiency of the flow battery. They found that high-performance systems can be designed in a way to minimize the pumping loss so that it is not the major loss mechanism, even while operating at high current densities. However, the flow field design itself is the major factor in the pressure drop [33]. Pressure drop data can be measured with a high degree of accuracy and precision and can be a useful tool for diagnostics [33,39,40]. However, the root cause of an increased pressure drop can be investigated via other means to be correlated to the flow behavior of the electrolyte inside the porous electrode.

This study aims to find beneficial effects on the saturation of a VRFB electrode by visualizing electrolyte wetting and quantifying saturation and pressure drop via injection of vanadium electrolytes species in different oxidation states into porous carbon electrodes with varying compression. Three-dimensional and two-dimensional X-ray based visualization techniques were performed to investigate the impact of thermal pre-treatment of carbon felt electrodes on the wetting behavior, the saturation, and the changes of the ECSA inside the porous electrode. The influence of compression and the electrolyte vanadium species on the initial wetting behavior, the saturation, and the pressure drop was analyzed and a parametric approach was performed to identify the impact of each effect. Both, quantitative and qualitative data are presented to highlight the effect of each parameter and for each test series, one quintessential set of results is presented, where similar effects were observed in a whole set of experiments.

2. Experimental

To investigate the effect of thermal activation (400 °C, 25 h), deionized water and 2 M sulfuric acid were injected into pristine and pre-treated carbon felt electrodes. A syringe pump was used to control the flow rate. Further, each vanadium electrolyte species (V(IV), V(V), V(II), V(III), all 0.1 M in 2 M H₂SO₄; the Roman numeral in brackets signifies the oxidation number of the vanadium species) was injected into dry activated carbon felt electrodes under different levels of compression (25%, 50%, and 70% reduction in thickness). After the initial injection at 15 μl min⁻¹, a continuous flow at 30 μl min⁻¹ was simulated for 300 s. Liquid movement in the sample was recorded via X-ray radiography, steady states were captured by X-ray tomography. Throughout the whole procedure, the flow pressure at the inlet was measured. This way, pressure data and saturation values after the imbibition and after continuous flow-through of the electrolyte were obtained for each combination of electrolyte species and compression ratio. The

experiments were performed at two separate synchrotron beamlines, the Canadian Light Source (CLS, Saskatoon, Canada) and the Karlsruhe Research Accelerator (KARA, Karlsruhe, Germany).

2.1. Injection and saturation experiments

To investigate the invasion behavior of the electrolyte, and the saturation during flow-through conditions, an injection device developed in-house was employed. The device is shown and explained in greater detail in earlier work, and it is constructed with a 0.45 mm flow channel on top of the sample chamber, which is functioning as an outlet [26]. Commercially available carbon felts (SIGRACELL® GFA 6 EA) from SGL Carbon (Meitingen, Germany) were thermally activated by preparing them in an oven under an air atmosphere at 400 °C for 25 h. This method introduces functional surface groups on the carbon fibers and increases the wettability of the carbon felt [29,41]. The verification of the change in wettability was achieved by injecting liquid into non-activated samples for comparison, as described in Section 3.1. The carbon felts were cut into a cylindrical shape with a diameter of 3 mm and mounted in the sample holder specifically designed for X-ray radiography and X-ray tomography experiments. A sketch of the sample holder is shown in Fig. 1 a). A syringe pump (Harvard Apparatus Model '11' plus) was connected to the electrolyte flow pipe on the stainless steel base of the sample holder to control the flow. The compression can be controlled by stacking stainless steel washers and incompressible polyethylene naphthalate (PEN) sheets (thickness verified by micrometer). The outer shell (dark gray) can be lifted independently from the inner shaft (light gray), which contains the electrolyte flow pipe. This way, the distance of the thin top part of the inner shaft to the screw-in top part equals the height of the stacked washers and PEN sheets and the desired compression can be variably chosen. The lowest compression was set to be a reduction of 25% in thickness compared to the thickness of the uncompressed felt, as it ensures a proper fit of the felt inside the sample holder without encouraging liquid flow around the sample in

contact with the walls of the sample holder. A compression of at least 25% is also beneficial in a cell setup, as it ensures adequate electrical contact of the electrode with the flow field collecting the current [21, 42]. Further, carbon felts compressed to 50% and 70% of their original thickness were investigated. The diameter of the inlet hole of the injection device, through which the liquid is pushed into the electrode, amounts to 0.25 mm. A close-up of the volume containing the electrolyte sample is shown in Fig. 1 b) and highlights the electrolyte inlet and outlet in greater detail. The outlet is designed to simulate a flow channel of a bipolar plate. Fig. 1 c) shows a representative pressure curve obtained by live monitoring the pressure during the injection. It displays the sequential procedure of the experiment, beginning with the initial set up of the starting condition, in which the liquid was pumped into the sample holder until it was close to the carbon felt at a through-plane position of $x = 0.0$ (A). When the liquid was between 5 and 10 mm away from coming in contact with the electrode, the flow was stopped to ensure that any residual overpressure was equilibrated and no further movement was detected. This process was controlled by X-ray live imaging and pressure monitoring (A-B). Before any liquid was injected into the electrode itself, a tomogram of the dry sample, further referenced as the dry scan, was recorded. After that point, the syringe pump was restarted with a flow rate of 15 $\mu\text{l min}^{-1}$ (B). Before the imbibition, a pressure build-up was observed during which the liquid was touching the surface of the carbon felt at a through-plane position of $x = 0.0$ (B-C) and the subsequent wicking of the liquid into the electrode corresponded with a steep pressure drop (C). At this point, the flow was immediately stopped and the pressure was allowed to equilibrate, which corresponds to the displacement of previously dry air pockets until no further movement in the sample is seen in the live imaging (C-D). The pressure build-up, the imbibition, and the first period of the equilibration are recorded as a radiography image stack with a frame rate of 12.5 (CLS) and 25.0 (KARA) frames per second (fps) for further quantitative analysis of the electrolyte invasion process. Once this steady state was reached, a second tomogram of the wet felt was recorded, further

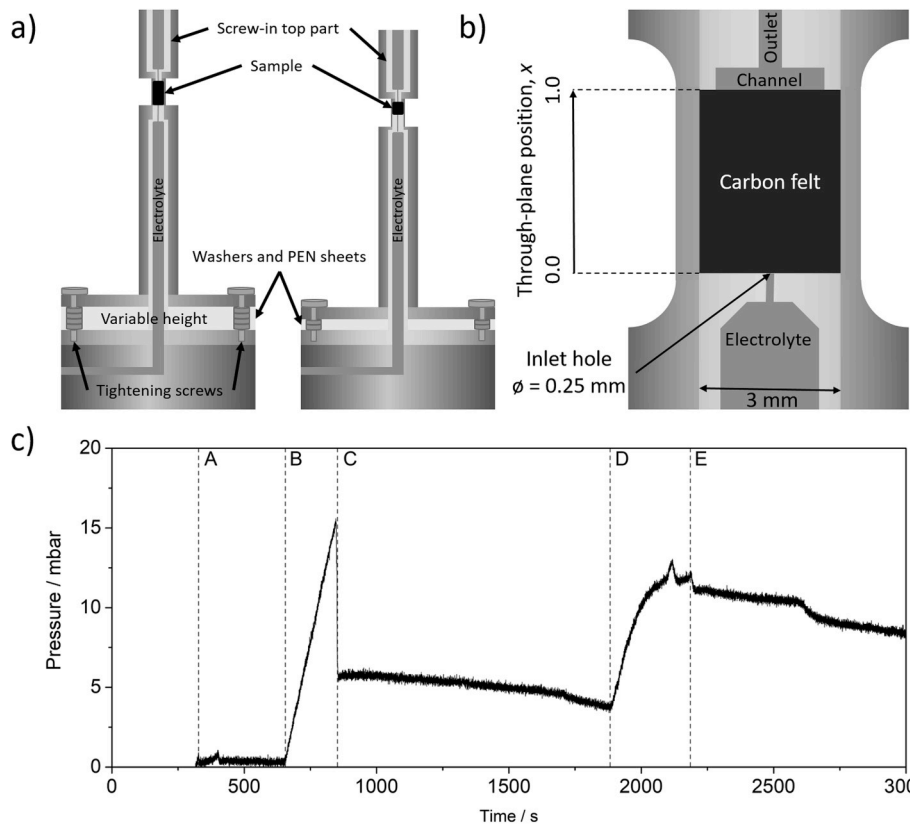


Fig. 1. a) Schematic drawing of the sample holder with special emphasis on the method of compression. The outer shell (dark gray) can be lifted independently from the inner shaft (light gray), which contains the electrolyte flow path, thus managing a controlled compression. b) Close-up of the volume containing the carbon electrode visualized in the experiments. c) Sample pressure curve recorded during the injection of electrolyte into porous carbon fiber. A–B: Pressure equilibration. B–C: Pressure build-up before imbibition (Point C) at 15 $\mu\text{l min}^{-1}$. C–D: Pressure equilibration before flow-through. D–E: Flow-through at 30 $\mu\text{l min}^{-1}$.

referenced as the wet scan. After the second tomography scan, flow-through conditions were simulated by setting the flow to $30 \mu\text{l min}^{-1}$ (D) for an additional 300 s (D-E), which was recorded via radiography. Another relaxation period was allowed and finally, the third tomogram was recorded to analyze the difference between the wetting before and after simulating flow-through conditions. After each completed injection experiment, the sample holder was dried off completely using compressed air and the sample was replaced, even when only switching to a higher compression ratio. This was done to ensure a completely dry starting point for each experiment and to eliminate hysteresis within the drainage and imbibition process.

2.2. Technical data of the synchrotron X-ray imaging

This work contains the results from two synchrotron facilities. Water and sulfuric acid were used as the invading electrolytes and the effect of carbon felt activation on the pressure drop and the saturation was investigated at CLS. Radiograms and tomograms were obtained at the Biomedical Imaging and Therapy Bending Magnet (BMIT-ID) 05ID-2 beamline at the Canadian Light Source Inc [43]. Radiograms were obtained at 12.5 fps and 80 ms exposure time at an effective pixel size of $6.5 \times 6.5 \mu\text{m}$. The beam energy was 30 keV at a current ranging between 150 mA and 220 mA. The transmitting photon flux was captured by a 10 μm thick Gadox scintillator screen coupled with a CMOS camera (OCAR-Flash 4.0, Hamamatsu Photonics, Shizuoka, Japan). Tomograms were recorded by taking dark and flat field images prior to each scan and then rotating the sample 180° around its vertical axis, taking 1250 images, one image every 0.14° . These images were subsequently reconstructed using the software NRecon (Bruker Corporation, USA) and converted into a three-dimensional grayscale image stack. After the data analysis was completed, thresholds were applied to omit noise in the 3D images and the contrast was enhanced to discern the multiple phases using the open-source imaging tool package FIJI® (based on ImageJ). The region around the sample resulted in bright artifacts when the background image was factored in. These bright spots were removed with the standard black and white threshold method in FIJI. Greyscale values greater than or equal to 254 were omitted, as this value did solely include the noise around the sample and did not affect the injected liquid inside the pore space. The FIJI auto-contrast feature was subsequently applied to enhance the visibility of the liquid distribution. The auto-contrast function was used to cut off greyscale values below 17 to improve the contrast between different thicknesses of the liquid column and to highlight the shape of the liquid distribution.

The compression study and the investigation of the wetting behavior of different electrolytes have been accomplished at the Topo-Tomo beamline (KARA). The mean energy of the polychromatic beam was 13.5 keV, the frame rate for radiography was 25 fps and the effective pixel size was $2.4 \times 2.4 \mu\text{m}$. A beam current greater than 70 mA was obtained throughout the whole imaging duration. The employed detector was a LuAg:Ce scintillator. Before every tomography, dark and flat field images were recorded and the resulting radiograms were corrected accordingly before reconstruction. Each tomogram entails 3000 single radiograms recorded while rotating the sample for 180° , corresponding to one snapshot every 0.06° .

2.3. Image analysis

The radiography images were analyzed with the Beer-Lambert law, similar to the work of Ge et al. [44]. This mathematical expression can be used to extract the local water thickness from an X-ray radiography image [17,45]. Applying the law to the radiograms obtained during the injection and flow-through experiments allows the quantitative analysis of the saturation inside the redox flow battery felts. As described by Ge et al., the Beer-Lambert law can be rearranged to give the local water thickness, as seen in Equation (1), where d_w is the water thickness, I_{dry} and I_{wet} are the respective local pixel intensities and μ_w is the X-ray

attenuation coefficient of the electrolyte [17], extracted from the NIST database [45].

$$d_w = \frac{\ln\left(\frac{I_{dry}}{I_{wet}}\right)}{\mu_w} \quad (1)$$

The Beer-Lambert law entails the assumption of a constant attenuation loss of the electrolyte and assumes a constant beam intensity throughout the whole experiment, as the attenuation is a function of the beam intensity. Extracting the local electrolyte thickness requires a dry reference image taken beforehand, which acts as the background. Taking a new background correction scan at the start of each scan allows the negligence of the decreasing synchrotron ring current over time. For radiography, the first 50 images before the electrolyte invasion are averaged to obtain a dry background image without electrolyte, by which the radiograms are divided to provide their local pixel intensities in the Beer-Lambert law. The radiography image stack is then analyzed using a python code written in-house, which applied the Beer-Lambert law to each pixel and yields their local thickness in the direction of the beam path. The saturation is calculated for five averaged slices (0.2 s) at the end of the pressure equilibration period when a steady state is reached and no changes in the image were observed anymore. In the case of the experiments at the white (polychromatic) beam at KARA, the water thickness was extracted relative to the background scan and then compared to a fully saturated image in order to determine the local thickness.

In the case of a tomography scan, the 3D image stack of the dry scan was used as the reference background. As there is no quantitative analysis of the tomograms, the background was subtracted to enhance the visibility of the features of the electrolyte column. The wet scan was subtracted from the tomogram after flow-through to highlight the qualitative differences of the liquid distribution within the pore space of the electrode before and after flow-through, with special emphasis on the air pocket displacement.

2.4. Preparation of the electrolytes

Vanadium (IV) electrolytes were freshly prepared by dissolving 0.1 M VOSO₄ (VOSO₄·5H₂O, chemically pure, GfE, Nuremberg, Germany) in 2 M H₂SO₄ (Suprapur, Merck, Darmstadt, Germany). To produce the vanadium (V) and vanadium (III) electrolytes, a VRFB in a redox flow test system (Scribner 857 test stand, Scribner Associates, North Carolina, USA) filled with vanadium (IV) electrolyte was charged until a charging current under 2 mA cm^{-2} was reached. After exchanging the vanadium (V) electrolyte in the charged VRFB with fresh vanadium (IV) electrolyte and subsequent re-charging, thereby the vanadium (II) electrolyte was obtained. The electrolytes were bottled, stored, and transported under argon atmosphere until they were inserted into the syringe right before the experiment.

3. Results and discussion

3.1. Effect of thermal carbon felt activation

The injection experiments were conducted with water and 2 M sulfuric acid on pristine and thermally activated electrodes to investigate the influence on the wettability and the pressure drop. The results show a significant difference in the liquid distribution inside the felt. In case of the non-activated carbon felt, the liquid preferentially moved along the walls of the sample holder rather than invading the hydrophobic pore space (Fig. 2 a) and c)). This is also apparent in the saturation numbers (Fig. 2 e)), which reach 12.0% (H₂O) and 33.5% (H₂SO₄) after wicking and 23.2% (H₂O) and 34.2% (H₂SO₄) after flow-through at $30 \mu\text{l min}^{-1}$ for the non-activated sample, shown in Fig. 2 a) and c). In case of the thermally activated sample, the saturation amounts to 80.2% (H₂O) and

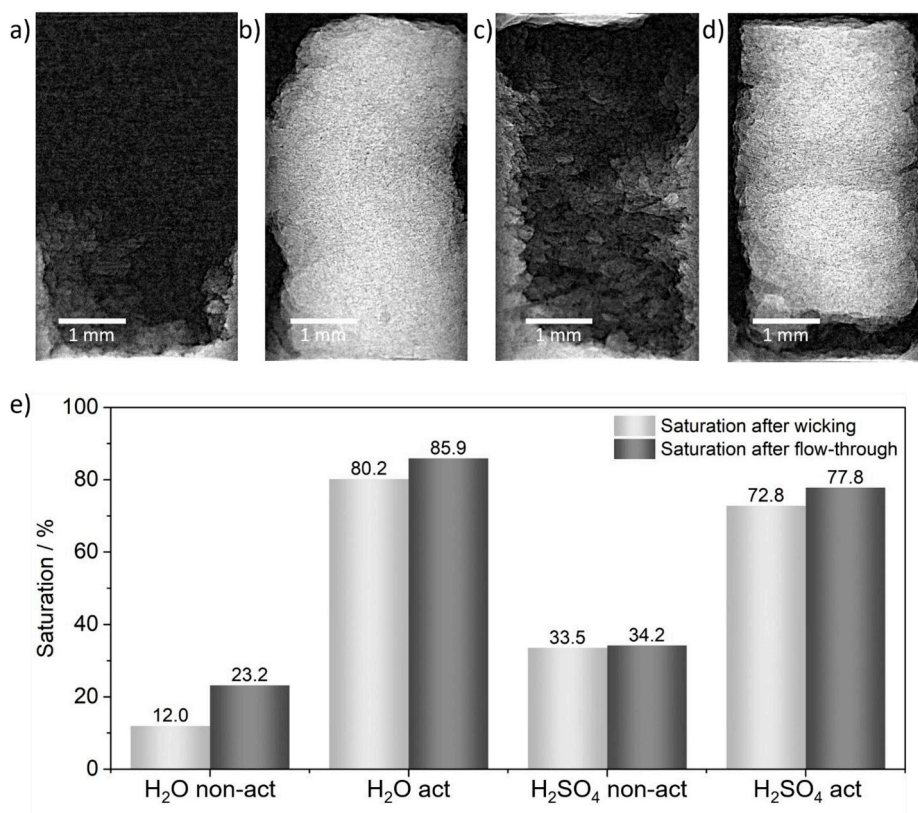


Fig. 2. Radiograms after initial imbibition of non-activated (a,c) and activated (b,d) carbon felt electrodes with H₂O (a,b) and H₂SO₄ (c,d) after the initial wetting. Light regions show liquid in the pore space. The brightness of the pixels corresponds to the thickness of the liquid in the beam path at that location. e) Corresponding saturation values of the entire porous electrode. The abbreviation *act* stands for thermally activated, *non-act* stands for not thermally activated.

72.8% (H₂SO₄) after wicking and 85.9% (H₂O) and 77.8% (H₂SO₄) after flow-through. The results show that after activation, the saturation increases by 200%–600%. This emphasizes the importance of activation of the carbon electrodes in VRFBs, as the introduced surface end groups and the oxygen content [5,29] largely increase the wettability and thus increase the ECSA available for the reaction. The effect of carbon combustion during an activation at 400 °C is largely outweighed by the introduction of surface groups on the carbon fibers, as described by Greco et al. [5]. Further, the recorded pressure drop is shown in Table 1. In case of the non-activated carbon felt, the liquid has to overcome a larger initial pressure before invading the felt or flowing around the electrode along the walls of the sample holder. The pressure drop decreases by a factor greater than two when employing an activated felt, thus reducing parasitic pumping losses significantly.

3.2. Injection characteristics and flow behavior

Five snapshots of injection experiments into an activated carbon felt at compression ratios of 25%, 50%, and 70% are shown in Fig. 3. The selected experiments are conducted with a V(IV) electrolyte, which shows the same qualitative characteristics as the other investigated electrolyte species. The imbibition is a quick process, taking less than 2 s in case of 25% compression and less than 1 s in case of 50% and 70% compression until the liquid reached the top of the sample and the

increase of the saturation slows down. The fast imbibition is due to the hydrophilic nature of the thermally pretreated felt electrode which wicks the electrolyte into the material as soon as the initial overpressure is reached and the liquid enters the pore space.

Throughout the whole injection at 25% and 50% compression, the phenomenon of capillary fingering above the invading electrolyte front can be observed, leading to the conclusion that capillary forces are dominating inside the electrode. Capillary fingering is observed in a capillary force dominated flow regimes when a favorable pathway for the invading liquid can be established. This pathway typically exhibits larger pores compared to its surrounding and higher pore connectivity, as these pores provide a lower entry pressure, thus allowing the liquid to invade the pore space ahead of the invasion front. Under a compression of 70%, the pores larger than 100 μm–150 μm are absent [21,46] and the capillary fingering is less pronounced. This effect might be amplified by the anisotropy in the arrangement of fibers in a carbon paper, as observed by Tariq et al. [22]. It can be assumed that the liquid which is preceding the invasion front is capillary force dominated. Further, Fig. 3 shows that at through-plane positions below 0.5 (bottom half of the sample) the saturation locally falls below 20%, presumably due to a shielding effect, as described by Jervis et al. [21]. They suggest a shielding effect, in which pore spaces of pores larger than the mean pore diameter of the carbon felt are inaccessible due to smaller surrounding pores with a high entry pressure. However, after the liquid was wicked into the porous electrode and the flow was switched off, the residual overpressure was large enough to overcome the shielding effect, invading the low porosity region.

The evolution of the saturation over time along with the through-plane position (from the injection face on the bottom (through-plane position $x = 0.0$) to the top of the felt (through-plane position $x = 1.0$)) is quantitatively highlighted in Fig. 4. Fig. 4 a) shows the imbibition at a compression of 25%, during which the felt initially saturates by wicking

Table 1

Comparison of the pressure drop inside thermally activated and pristine samples for injections with H₂O and H₂SO₄.

	Activated sample	Non-activated sample
Pressure drop/mbar (H ₂ O)	14.5	28.9
Pressure drop/mbar (H ₂ SO ₄)	12.9	32.1

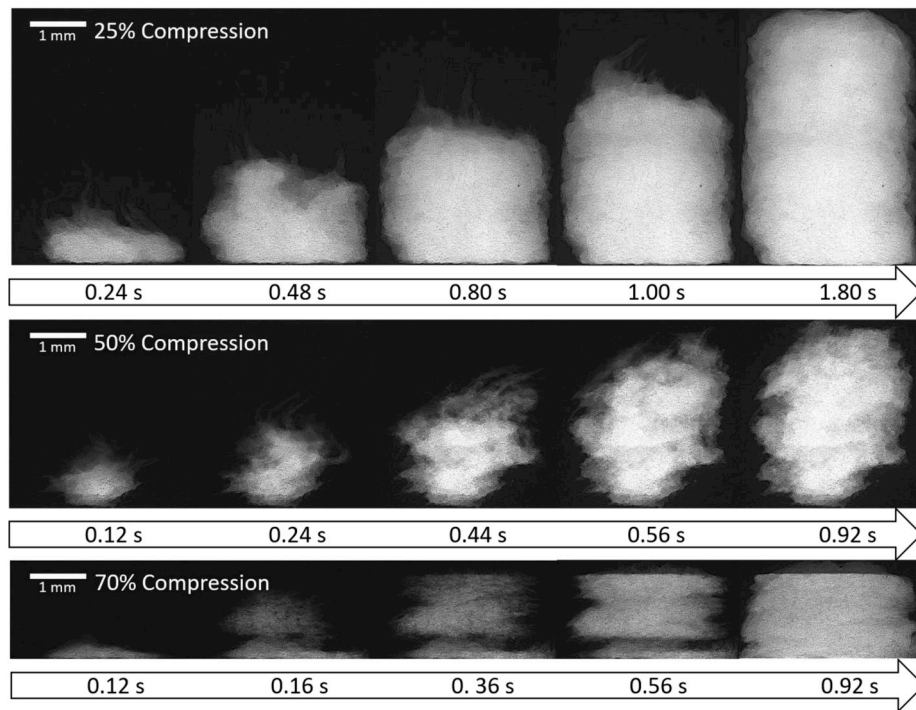


Fig. 3. Selected radiograms during wicking of electrolyte with respective time frames given in the time scale given in the time scale below each image. Each row represents one compression ratio shown in the top left. The images were obtained after background subtraction and contrast enhancement.

the electrolyte. The steep vertical decrease in the lines represents the invasion front. As the lines are temporally equidistant, the horizontal separation of the lines shows the flow velocity of the liquid at any given time. Higher proximity of the steep decrease of the lines signifies a slower the movement of the invasion front. Thus, the imbibition slows down with time before it reaches a steady state. This is in agreement with the modeled predictions of Banerjee et al., which showed that with increasing saturation, the available wicking pressure decreases, which would result in a decreased rate of imbibition [46]. Further, it is

apparent that at high through-plane positions $x > 0.95$, some regions are not wetted, leading to a local decrease in saturation to less than 60%. Even during the pressure equilibration after the pressure drop, these regions do not saturate, as the liquid preferentially exits the pore space into the flow channel on top of the sample. Fig. 4 b) shows the saturation curves during the flow-through experiment. The graph describing the saturation at 0 s in Fig. 4 b) is similar to the graph at 1.8 s in Fig. 4 a), even though it represents the saturation after the pressure relaxation period. The similarity of these curves shows that the saturation did not

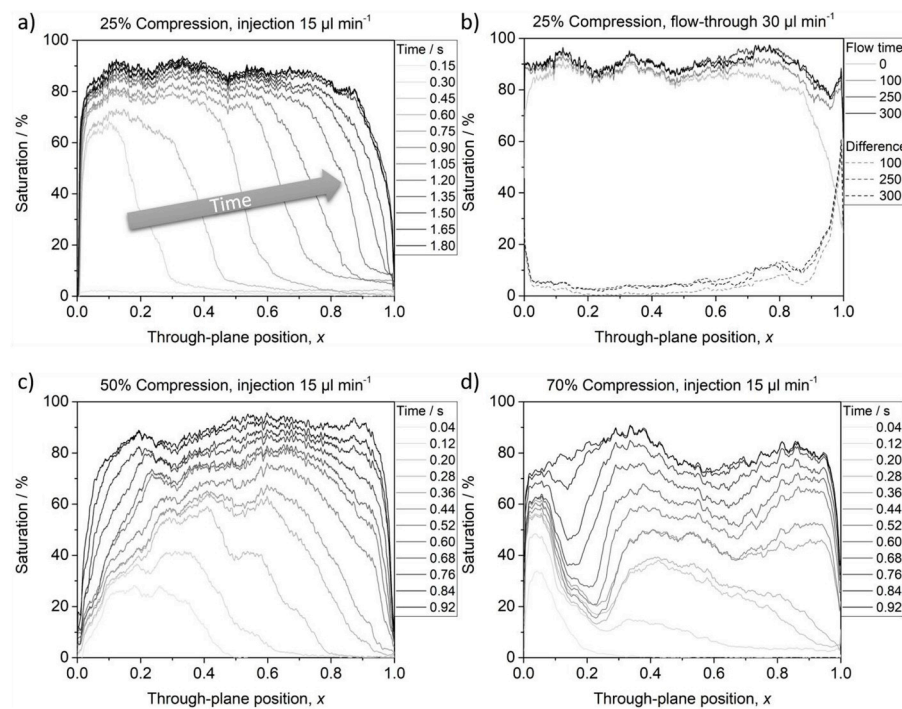


Fig. 4. a) Temporally equidistant saturation curves plotted over through-plane position (from $x = 0.0$: injection hole to $x = 1.0$: top of felt facing flow channel outlet) over time during initial imbibition. After 1.80 s, the breakthrough was observed and the flow was stopped. b) Saturation curves over the through-plane position during continuous flow-through operation at $30 \mu\text{l min}^{-1}$. The solid lines show the saturation curves after a given time of flow-through operation. The solid line labeled *Flow time* = 0 s represents the initial saturation profile at the start of flow-through. The dashed lines show the differential increase of saturation with respect to the solid line (*Flow time* = 0 s) after a given time of flow-through operation (*Difference*/s). The difference refers to the local increase of saturation at a given through-plane position, x , the time in seconds indicates how much time of flow-through operation has passed. c) Saturation curves plotted similar to a), under 50% compression of the carbon felt electrode. d) Saturation curves plotted similar to a) and c), under 70% compression. The filling of shielded pores is visible at through-plane positions between $0.1 < x < 0.3$.

change significantly during the pressure equilibration. Fig. 4 b) highlights that after 100 s of flow-through at $30 \mu\text{l min}^{-1}$, the saturation decrease at high through-plane positions is absent and that the saturation is greater than 70% for through-plane positions $x > 0.95$, implying that the pressure in the liquid column exceeds the capillary pressure of these pore spaces, saturating them before the pressure can be equilibrated by forcing the liquid out on top of the sample into the channel. Until 250 s into the flow-through operation, the saturation increases, steadily saturating more pores. However, in the last 50 s, there is a net decrease in saturation of through-plane positions $x > 0.6$. This can be explained by a droplet of electrolyte coming in contact with the hydrophilic wall of the flow channel on top of the sample, which draws out the liquid and pushes the remaining air from above the electrode inside the flow channel into the pores. The bottom half of the sample is not affected by this effect, as the saturation curves do not change notably in that region. Fig. 4 c) shows the imbibition at a compression of 50%. Similar to Fig. 4 a), the movement of the bulk of the electrolyte slows down with time and a steep decrease in saturation at high through-plane positions is visible. However, the decrease to 60% local saturation and below occurs at through-plane positions of $x > 0.98$, which is higher than for 25% compression. Fig. 4 d) describes the imbibition of an electrode compressed to 70%. A local minimum occurring at through-plane positions between $0.1 > x > 0.3$ highlights the aforementioned shielding effect and it can be seen that the affected volume is saturated by the residual overpressure over time. After less than 1 s, the minimum is absent.

3.3. Influence of compression and vanadium species on the flow-through pressure drop

Fig. 5 shows that increasing the compression ratio from 25% to 70%, the pressure drop at flow-through conditions increases by 401.2%. Raising the compression from 25% to 50% affects the flow-through pressure less (average pressure increases by 87.2%) than raising the compression from 50% to 70% (average pressure increase by 214.3%), as, in accordance with Banerjee et al., the number of pores larger than the mean pore size decreases rapidly with higher compression [24]. The results shown in Fig. 5 conclude, that at 50% compression, pores larger than the mean pore diameter are still available to establish a stable flow-through at $30 \mu\text{l min}^{-1}$ while maintaining a lower pressure drop. However, at a compression ratio of 70%, the pores larger than $150 \mu\text{m}$ are absent, as they collapse first and the liquid pathway has to include smaller pores compared to the uncompressed sample, thus increasing the

pressure drop significantly. The pressure increase was less dominant on the V(II) and the V(V) electrolyte. This observation can be explained by a lower dynamic viscosity of the V(II) and the V(V) electrolyte species, as described by Xu et al., who calculated a decreasing dynamic viscosity for an increasing SoC in a VRFB, which results in a lower pressure drop for V(II) and V(V) electrolyte species [37]. However, a strong dependence of the pressure on the volume immediately surrounding the inlet hole cannot be excluded in this setup. Poor connectivity of pores and small pore diameters below $25 \mu\text{m}$ in the vicinity of the inlet will increase the pressure, which might dominate the influence of the electrolyte species on the pressure drop, especially as the porosity is lower in the region closest to the compressive element of the sample holder, as reported by Jervis et al. [21]. As described earlier, modeled mercury intrusion porosimetry experiments by Jervis et al. suggest a high number of shielded pores inside the unevenly compressed carbon felts [21]. Thus, the increased wettability of V(II) and V(V) is detrimental in overcoming local porosity differences and decreasing the pressure drop.

3.4. Influence of compression and vanadium species on the saturation

The influence of compression on the saturation of different vanadium species inside the electrolyte is presented in Fig. 6. Increasing the compression ratio from 25% to 50% does not affect the saturation, whereas a compression ratio of 70% decreases the average saturation by 11.2% (compared to 25% compression). The oxidation number of the vanadium species plays a minor role in the saturation of the electrode. The average deviation from the medium saturation amounts to 3.0% at a compression ratio of 25%, 2.0% at a compression ratio of 50%, and 4.7% at 70% compression. The fine difference between the vanadium species

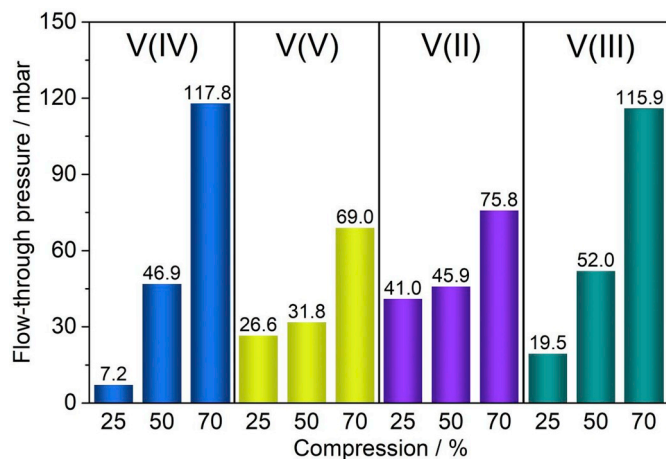


Fig. 5. Injection pressure at $30 \mu\text{l min}^{-1}$ flow-through conditions for different electrolyte species at given levels of compression, as denoted by the x-axis tick labeling. The respective vanadium species is shown above the bars. In addition, the bar color indicates the various vanadium species.

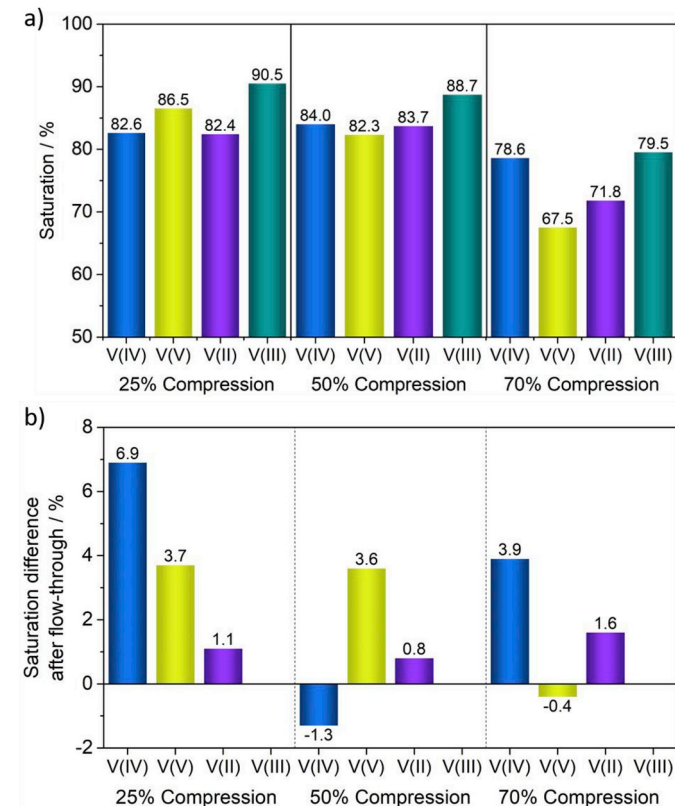


Fig. 6. a) Saturation values after the initial imbibition at $15 \mu\text{l min}^{-1}$ for each level of compression and each respective electrolyte species. In addition to the x-axis tick labels, the bar color indicates the various vanadium species. b) The difference in saturation before and after 300 s flow-through at $30 \mu\text{l min}^{-1}$. *No information about saturation after flow-through for V(III) electrolyte due to technical difficulties at the synchrotron.

is not showing a discernible trend in the final saturation. Even at the highest compression, the flow behavior is affected more strongly by the surface properties and the structure of the electrode rather than the wetting properties of the vanadium species in the electrolyte. At each compression level, V(III) shows the highest saturation inside the carbon felt, as seen in Fig. 6 a). However, this difference still plays a minor role compared to the overall effect of compression. Similar results are found in case of the flow-through saturation at $30 \mu\text{l min}^{-1}$ in Fig. 6 b). Fig. 6 b) does not contain flow-through values for V(III) (see figure description). The average increase of the saturation after flow-through with $30 \mu\text{l min}^{-1}$ amounts to 2.2% (varies between negative 1.3% and 6.9%). This minor difference further emphasizes the critical importance of the initial wetting properties of the felt, as this factor plays a major role in the saturation. However, the impact of the vanadium species might change if an electrical field is applied.

3.5. Internal structure of the liquid pathway

As described in Section 3.4, the saturation values of the investigated vanadium species do not deviate by more than 5% from the average electrolyte saturation, as the flow behavior is dominated by the surface properties and the structure of the carbon felt. Fig. 7 shows a tomographic slice of each of the injected electrolytes inside the sample holder at a through-plane position of $x = 0.5$. They all show similar characteristics, most notably the occurrence of trapped air bubbles, the cause of which is assumed to be the Cassie-Baxter effect, which describes the formation of enclosed air bubbles inside the liquid column on a rough surface, as previously described by Greco et al. [5]. This effect is observed with all investigated vanadium electrolyte species and when comparing the initial imbibition with the flow-through experiment, some of the air bubbles are displaced by liquid after flow-through, but the majority is persistent, as shown in Fig. 8.

Further worth noting is the formation of new air bubbles inside the electrolyte column during flow-through. This process occurs at higher

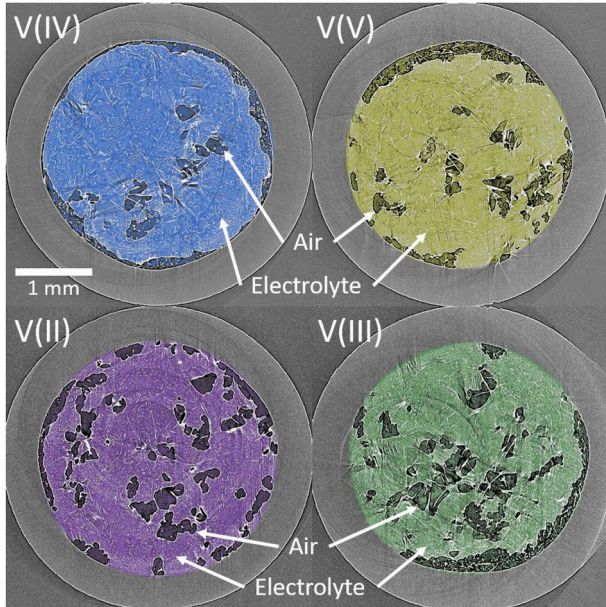


Fig. 7. Tomograms were taken after the equilibration period after the injection of electrolyte into the porous electrode. The tomograms are sliced at a through-plane position of $x = 0.5$, corresponding to 50% of the total height of the compressed electrode (25% compression). The images show the internal structure of the liquid column inside the carbon felt. The colors indicate the color of the respective vanadium species. The air pockets are represented in a darker tone of color. The arrows indicate a region of air or electrolyte as reference.

through-plane positions, where air trapped in the channel structure above the sample can be pushed back into the sample when a droplet of the wetting electrolyte touches the wall of the sample holder and gets wicked out of the sample, replacing the liquid of saturated pores with air, as explained in Section 3.2. The main reason for the increased saturation after flow-through is the expansion of the liquid pathway to accommodate the flux through the electrode, further saturating previously dry pores. This result shows that not only capillary forces are acting during flow-through at $30 \mu\text{l min}^{-1}$. These findings are in agreement with Tariq et al., who investigated the electrolyte distribution in a carbon paper-based material and claim that after a node-to-node transport mechanism, the electrolyte invades smaller pores around the initially wetted volume. They suggest that, due to an inhomogeneous use of the electrode, the presence of trapped air bubbles accelerates degradation once a current is applied [22]. Another reason for the increased saturation after flow-through is the contact of the liquid column with the hydrophilic wall of the sample holder, as can be seen in Fig. 8. Once the electrolyte reaches the wall, a thorough contact is established and the local saturation increases along the contact area.

Additionally, one experiment was conducted with two flow-through periods at $30 \mu\text{l min}^{-1}$, showing that additional air pockets have been displaced, but the saturation only increased by an additional 1.1% in case of H_2SO_4 as the electrolyte. The persistence of trapped air bubbles prevents the carbon felt from reaching 100% saturation at these flow conditions. Longer experiments are necessary to investigate the effect of continuous long-term operation on the air displacement inside a carbon felt.

4. Concluding remarks

In this work, the wetting behavior of activated and non-activated carbon felts was investigated and it was observed that the introduction of surface groups during thermal activation significantly facilitates a thorough wetting, leading to a higher saturation inside the carbon felt and thus to an overall higher ECSA, which should theoretically improve the performance of the VRFB. With sulfuric acid as the electrolyte, the saturation increased up to six times at a compression ratio of 25%. The pressure drop decreases by a factor of two in case of a thermally activated felt, which decreases the ancillary pumping losses significantly and further highlights the importance of thermal activation of the carbon felt electrode.

Further, the influence of compression on the pressure drop was investigated. The pressure drop increases with higher compression ratios. The increase in the pressure drop between compression ratios of 25% and 50% was less pronounced (87.2%) than the difference between 50% and 70% (214.3%).

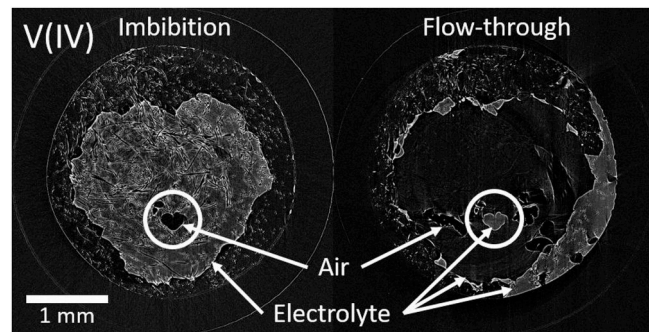


Fig. 8. a) High contrast tomogram (V(IV)) in activated carbon felt, through-plane position $x = 0.2$; 1.0 mm below the flow-channel on top of the sample) recorded after the equilibration period subsequent to the initial wetting, exhibiting an air pocket circled in white. b) Image obtained by subtraction of the steady-state of the initial wetting (Fig. 8 a) from the image after flow-through. The same position is shown and the circled area highlights that the air pocket is now filled with electrolyte (brighter shade of gray). New, additional air pockets have formed as well.

The analysis of the three-dimensional tomograms yielded insight into the internal structure of the liquid column inside the porous electrode. The enclosure of air pockets was observed and the displacement of a fraction of air pockets after flow-through has been shown. At high through-plane positions close to the flow channel on the opposite side of the injection hole, the formation of new air pockets is observed. This can be explained by the displacement of air from the flow channel back into the pores of the carbon felt when the electrolyte comes in contact with the hydrophilic channel on the top and emerges from the sample.

Furthermore, the initial saturation after imbibition at $15 \mu\text{L min}^{-1}$ was compared to the saturation after flow-through at $30 \mu\text{L min}^{-1}$ for 300 s and it was found that the saturation increase averages at 2.2%. A second flow-through period further increased the saturation of the pore space by 1.1% to total saturation of 78.9%. This shows that the majority of trapped air bubbles in the liquid column persists and emphasizes the importance of the initial wettability of the carbon felt, which is directly linked to the surface properties. The presence of trapped air prevents the felt from reaching 100% saturation, which might accelerate the degradation due to local inhomogeneity of the electrical field.

Acknowledgments

This work contributes to the research performed at CELEST (Center for Electrochemical Energy Storage Ulm-Karlsruhe). Financial support from the “Impuls- und Vernetzungsfonds der Helmholtz Gesellschaft” (Young Investigator Group project VH-NG-616), the Karlsruhe House of Young Scientists (KHYS), and the Deutscher Akademischer Austauschdienst (DAAD) with regard to the International Collaboration Package is greatly acknowledged. Further, the authors would like to thank the ZSW (Zentrum für Sonnenenergie und Wasserstoff-Forschung) for the use of the computational equipment. This study was further supported by Ning Zhu, Sergey Gasilov, Denise Miller, and the Biomedical Imaging and Therapy (BMIT) beamline staff as well as ChungHyuk Lee of the Thermofluids for Energy and Advanced Materials (TEAM) laboratory of the University of Toronto. Additionally, we gratefully acknowledge SGL Carbon for the supply of SIGRACELL® carbon felts.

We acknowledge the KIT light source for the provision of instruments at their beamlines and we would like to thank the Institute for Beam Physics and Technology (IBPT) for the operation of the storage ring, the Karlsruhe Research Accelerator (KARA).

Research described in this paper was performed at the Canadian Light Source, which is supported by the Canada Foundation for Innovation, Natural Sciences and Engineering Research Council of Canada, the University of Saskatchewan, the Government of Saskatchewan, Western Economic Diversification Canada, the National Research Council Canada, and the Canadian Institutes of Health Research.

Glossary

(II), (III), (IV), (V)	Oxidation numbers of vanadium (given in roman numerals)
VRFB	Vanadium redox flow battery
RFB	Redox flow battery
ECSA	Electrochemically active surface area
UV-VIS	Ultraviolet-visible light spectroscopy
PEMFC	Polymer electrolyte membrane fuel cell
XPS	X-ray photoelectron spectroscopy
H_2SO_4	Sulfuric acid
M	Molar given in mol L^{-1}
CLS	Canadian Light Source
KARA	Karlsruhe Research Accelerator
PEN	Polyethylene naphthalate
VOSO ₄	Vanadyl sulphate
H_2O	Water
x	Through-plane position inside the carbon felt electrode

References

- [1] B. Dunn, H. Kamath, J.-M. Tarascon, Electrical energy storage for the grid: a battery of choices, *Science* 334 (2011) 928–935.
- [2] P.A. EPRI, CA, the U.S. Department of Energy, 1001834, EPRI-DOE Handbook of Energy Storage for Transmission & Distribution Applications, Washington, DC, 2003.
- [3] A.Z. Weber, M.M. Mench, J.P. Meyers, P.N. Ross, J.T. Gostick, Q. Liu, Redox flow batteries: a review, *J. Appl. Electrochem.* 41 (2011) 1137.
- [4] K.J. Kim, M.-S. Park, Y.-J. Kim, J.H. Kim, S.X. Dou, M. Skyllas-Kazacos, A technology review of electrodes and reaction mechanisms in vanadium redox flow batteries, *J. Mater. Chem. A* 3 (2015) 16913–16933.
- [5] K.V. Greco, A. Forner-Cuenca, A. Mularczyk, J.J. Eller, F.R. Brushett, Elucidating the nuanced effects of thermal pretreatment on carbon paper electrodes for vanadium redox flow batteries, *ACS Appl. Mater. Interfaces* 10 (2018) 44430–44442.
- [6] T.J. Rabbow, M. Trampert, P. Pokorny, P. Binder, A.H. Whitehead, Variability within a single type of polyacrylonitrile-based graphite felt after thermal treatment. Part I: physical properties, *Electrochim. Acta* 173 (2015) 17–23.
- [7] Y.A. Gandomi, D.S. Aaron, J.R. Houser, M.C. Daugherty, J.T. Clement, A. M. Pezeshki, T.Y. Ertugrul, D.P. Moseley, M.M. Mench, Critical review - experimental diagnostics and material characterization techniques used on redox flow batteries, *J. Electrochim. Soc.* 165 (2018) A970–A1010.
- [8] Q.H. Liu, G.M. Grim, A.B. Papandrew, A. Turhan, T.A. Zawodzinski, M.M. Mench, High performance vanadium redox flow batteries with optimized electrode configuration and membrane selection, *J. Electrochim. Soc.* 159 (2012) A1246–A1252.
- [9] K. Oh, T.J. Kang, S. Park, M.C. Tucker, A.Z. Weber, H. Ju, Effect of flow-field structure on discharging and charging behavior of hydrogen/bromine redox flow batteries, *Electrochim. Acta* 230 (2017) 160–173.
- [10] Q. Xu, T.S. Zhao, C. Zhang, Performance of a vanadium redox flow battery with and without flow fields, *Electrochim. Acta* 142 (2014) 61–67.
- [11] S. Kim, E. Thomsen, G. Xia, Z. Nie, J. Bao, K. Recknagle, W. Wang, V. Viswanathan, Q. Luo, X. Wei, A. Crawford, G. Coffey, G. Maupin, V. Sprenkle, 1 kW/1 kWh advanced vanadium redox flow battery utilizing mixed acid electrolytes, *J. Power Sources* 237 (2013) 300–309.
- [12] L. Tong, Q. Chen, A.A. Wong, R. Gómez-Bombarelli, A. Aspuru-Guzik, R.G. Gordon, M.J. Aziz, UV-Vis spectrophotometry of quinone flow battery electrolyte for in situ monitoring and improved electrochemical modeling of potential and quinhydrone formation, *Phys. Chem. Chem. Phys.* 19 (2017) 31684–31691.
- [13] D.S. Hussey, D.L. Jacobson, M. Arif, J.P. Owejan, J.J. Gagliardo, T.A. Trabold, Neutron images of the through-plane water distribution of an operating PEM fuel cell, *J. Power Sources* 172 (2007) 225–228.
- [14] P. Boillat, J. Biesdorf, P. Oberholzer, A. Kaestner, T.J. Schmidt, Evaluation of neutron imaging for measuring phosphoric acid distribution in high temperature PEFCs, *J. Electrochim. Soc.* 161 (2014) F192–F198.
- [15] S. Chevalier, N. Ge, J. Lee, R. Banerjee, H. Liu, M. George, P. Shrestha, D. Muirhead, J. Hinebaugh, Y. Tabuchi, T. Kotaka, A. Bazylak, Synchrotron X-ray radiography as a highly precise and accurate method for measuring the spatial distribution of liquid water in operating PEM fuel cells, *J. Electrochim. Soc.* 164 (2017) F107–F114.
- [16] S. Chevalier, J. Lee, N. Ge, R. Yip, P. Antonacci, Y. Tabuchi, T. Kotaka, A. Bazylak, In operando measurements of liquid water saturation distributions and effective diffusivities of polymer electrolyte membrane fuel cell gas diffusion layers, *Electrochim. Acta* 210 (2016) 792–803.
- [17] N. Ge, S. Chevalier, J. Hinebaugh, R. Yip, J. Lee, P. Antonacci, T. Kotaka, Y. Tabuchi, A. Bazylak, Calibrating the X-ray attenuation of liquid water and correcting sample movement artefacts during in operando synchrotron X-ray radiographic imaging of polymer electrolyte membrane fuel cells, *J. Synchrotron Radiat.* 23 (2016) 590–599.
- [18] J. Lee, S. Chevalier, R. Banerjee, P. Antonacci, N. Ge, R. Yip, T. Kotaka, Y. Tabuchi, A. Bazylak, Investigating the effects of gas diffusion layer substrate thickness on polymer electrolyte membrane fuel cell performance via synchrotron X-ray radiography, *Electrochim. Acta* 236 (2017) 161–170.
- [19] J. Eller, J. Roth, F. Marone, M. Stampanoni, F.N. Büchi, Operando properties of gas diffusion layers: saturation and liquid permeability, *J. Electrochim. Soc.* 164 (2017) F115–F126.
- [20] R. Banerjee, N. Ge, C. Han, J. Lee, M.G. George, H. Liu, D. Muirhead, P. Shrestha, A. Bazylak, Identifying in operando changes in membrane hydration in polymer electrolyte membrane fuel cells using synchrotron X-ray radiography, *Int. J. Hydrogen Energy* 43 (2018) 9757–9769.
- [21] R. Jervis, M.D.R. Kok, T.P. Neville, Q. Meyer, L.D. Brown, F. Iacoviello, J. T. Gostick, D.J.L. Brett, P.R. Shearing, In situ compression and X-ray computed tomography of flow battery electrodes, *J. Energy Chem.* 27 (2018) 1353–1361.
- [22] F. Tariq, J. Rubio-Garcia, V. Yufit, A. Bertei, B.K. Chakrabarti, A. Kucernak, N. P. Brandon, Uncovering the mechanisms of electrolyte permeation in porous electrodes for redox flow batteries through real time in situ 3D imaging, *Sustain. Energy Fuels* 2 (2018) 2068–2080.
- [23] L. Chen, Y. He, W.-Q. Tao, P. Zelenay, R. Mukundan, Q. Kang, Pore-scale study of multiphase reactive transport in fibrous electrodes of vanadium redox flow batteries, *Electrochim. Acta* 248 (2017) 425–439.
- [24] R. Banerjee, N. Bevilacqua, L. Eifert, R. Zeis, Characterization of carbon felt electrodes for vanadium redox flow batteries - a pore network modeling approach, *J. Energy Storage* 21 (2019) 163–171.

- [25] S. Chevalier, M. Fazeli, F. Mack, S. Galbiati, I. Manke, A. Bazylak, R. Zeis, Role of the microporous layer in the redistribution of phosphoric acid in high temperature PEM fuel cell gas diffusion electrodes, *Electrochim. Acta* 212 (2016) 187–194.
- [26] N. Bevilacqua, M.G. George, S. Galbiati, A. Bazylak, R. Zeis, Phosphoric acid invasion in high temperature PEM fuel cell gas diffusion layers, *Electrochim. Acta* 257 (2017) 89–98.
- [27] E.A. Wargo, T. Kotoka, Y. Tabuchi, E.C. Kumbur, Comparison of focused ion beam versus nano-scale X-ray computed tomography for resolving 3-D microstructures of porous fuel cell materials, *J. Power Sources* 241 (2013) 608–618.
- [28] P. Trogadas, O.O. Taiwo, B. Tjaden, T.P. Neville, S. Yun, J. Parrondo, V. Ramani, M.-O. Coppens, D.J.L. Brett, P.R. Shearing, X-ray micro-tomography as a diagnostic tool for the electrode degradation in vanadium redox flow batteries, *Electrochim. Commun.* 48 (2014) 155–159.
- [29] L. Eifert, R. Banerjee, Z. Jusys, R. Zeis, Characterization of carbon felt electrodes for vanadium redox flow batteries: impact of treatment methods, *J. Electrochem. Soc.* 165 (2018) A2577–A2586.
- [30] J.T. Clement, Investigation of Localized Performance and Gas Evolution in All-Vanadium Redox Flow Batteries via In-Situ Distributed Diagnostic Techniques, Ph. D. diss., University of Tennessee, 2016.
- [31] A. Tang, J. Bao, M. Skyllas-Kazacos, Studies on pressure losses and flow rate optimization in vanadium redox flow battery, *J. Power Sources* 248 (2014) 154–162.
- [32] X.L. Zhou, T.S. Zhao, L. An, Y.K. Zeng, L. Wei, Critical transport issues for improving the performance of aqueous redox flow batteries, *J. Power Sources* 339 (2017) 1–12.
- [33] J.R. Houser, A.M. Pezeshki, J.T. Clement, D.S. Aaron, M.M. Mench, Architecture for improved mass transport and system performance in redox flow batteries, *J. Power Sources* 351 (2017) 96–105.
- [34] D. Reed, E. Thomsen, B. Li, W. Wang, Z. Nie, B. Koeppel, V. Sprenkle, Performance of a low cost interdigitated flow design on a 1 kW class all vanadium mixed acid redox flow battery, *J. Power Sources* 306 (2016) 24–31.
- [35] L. Zeng, T. Zhao, W. L, Revealing the performance enhancement of oxygenated carbonaceous materials for vanadium redox flow batteries: functional groups or specific surface area? *Adv. Sustain. Syst.* 2 (2018), 1700148.
- [36] Z. He, Z. Chen, W. Meng, Y. Jiang, G. Cheng, L. Dai, L. Wang, Modified carbon cloth as positive electrode with high electrochemical performance for vanadium redox flow batteries, *J. Energy Chem.* 25 (2016) 720–725.
- [37] Q. Xu, T.S. Zhao, C. Zhang, Effects of SOC-dependent electrolyte viscosity on performance of vanadium redox flow batteries, *Appl. Energy* 130 (2014) 139–147.
- [38] T.J. Latha, S. Jayanti, Hydrodynamic analysis of flow fields for redox flow battery applications, *J. Appl. Electrochem.* 44 (2014) 995–1006.
- [39] R. Banerjee, D. Howe, V. Mejia, S.G. Kandlikar, Experimental validation of two-phase pressure drop multiplier as a diagnostic tool for characterizing PEM fuel cell performance, *Int. J. Hydrogen Energy* 39 (2014) 17781–17801.
- [40] A.M. Pezeshki, R.L. Sacci, F.M. Delnick, D.S. Aaron, M.M. Mench, Elucidating effects of cell architecture, electrode material, and solution composition on overpotentials in redox flow batteries, *Electrochim. Acta* 229 (2017) 261–270.
- [41] B. Sun, M. Skyllas-Kazacos, Modification of graphite electrode materials for vanadium redox flow battery application - I. Thermal treatment, *Electrochim. Acta* 37 (1992) 1253–1260.
- [42] T.-C. Chang, J.-P. Zhang, Y.-K. Fuh, Electrical, mechanical and morphological properties of compressed carbon felt electrodes in vanadium redox flow battery, *J. Power Sources* 245 (2014) 66–75.
- [43] T.W. Wysokinski, D. Chapman, G. Adams, M. Renier, P. Suortti, W. Thomlinson, Beamlines of the biomedical imaging and therapy facility at the Canadian light source - Part 1, *Nucl. Instrum. Methods Phys. Res., Sect. A* 582 (2007) 73–76.
- [44] S.-J. Lee, S.-G. Kim, G.-G. Park, C.-S. Kim, Quantitative visualization of temporal water evolution in an operating polymer electrolyte fuel cell, *Int. J. Hydrogen Energy* 35 (2010) 10457–10463.
- [45] J.H. Hubbell, S.M. Seltzer, Tables of X-Ray Mass Attenuation Coefficients and Mass Energy-Absorption Coefficients from 1 keV to 20 MeV for Elements Z = 1 to 92 and 48 Additional Substances of Disimetric Interest, 2004.
- [46] R. Banerjee, N. Bevilacqua, A. Mohseninia, B. Wiedemann, F. Wilhelm, J. Scholten, R. Zeis, Carbon felt electrodes for redox flow battery: impact of compression on transport properties, *J. Energy Storage* (2019). Prepared Manuscript.